JOURNAL OF THERMOPHYSICS AND HEAT TRANSFER
Vol. 22, No. 4, October–December 2008

Aerothermodynamic Study of Ultrahigh-Temperature Ceramic Winglet for Atmospheric Reentry Test

Raffaele Savino* and Mario De Stefano Fumo†
University of Naples "Federico II,"
80125 Naples, Italy

DOI: 10.2514/1.33296

This paper deals with the aerothermodynamic analysis of an advanced concept of hot structure to be investigated at atmospheric reentry conditions. The paper gives a general description of the hot structure architecture and performs an aerothermodynamic analysis to optimize the winglet configuration, based on an ultrahigh-temperature ceramics leading edge able to withstand very high temperatures. Three-dimensional fluid-dynamic computations are carried out to evaluate the aerothermal loads on the winglet. The physical model includes viscous effects, real gas properties, nonequilibrium chemical reactions and surface catalytic effects. The numerical model has been validated by experimental results of two- and three-dimensional hypersonic flowfields. A thermal model of the structure has been implemented to predict the temperature of the winglet during reentry. The results are discussed with reference to the effects of the thermal interaction with the capsule skin, the relevance of thermal conduction inside the structure, and the transient methodology. The effect of different assumptions on the ultrahigh-temperature ceramics catalytic properties is discussed.

Nomenclature

C	=	species mass fraction
C_f	=	skin friction coefficient
c_p	=	specific heat, J/kg · K
D	=	species diffusivity, m^2 s
H_0	=	specific total enthalpy, J/kg
K	=	material catalytic constant, m/s
M_∞	=	freestream Mach number
m	=	species molecular weight
p_0	=	total pressure, Pa
$\dot{q}_c$	=	convective surface heat flux, W/m^2
$\dot{q}_{\text{in}}$	=	surface heat flux entering the structure, W/m^2
$\dot{q}_n$	=	normalized heat flux
$\dot{q}_{\text{sp}}$	=	stagnation point heat flux, W/m^2
R_0	=	universal gas constant, J/K · mol
T_w	=	temperature, K
T_∞	=	freestream temperature, K
γ	=	catalytic recombination factor
ε	=	surface emissivity
σ	=	Stephen–Boltzmann constant, $W/m^2 \cdot K^4$

I. Introduction

THE European Space Agency is pursuing the European experimental reentry test bed (EXPERT) hypersonic flight test program to give unique opportunities to improve knowledge of challenging problems of hypersonic flight [1]. The configuration chosen for the EXPERT vehicle is basically a blunt cone with four flaps and flat surfaces ahead of them. The vehicle will be launched by the Russian Volna launcher and will make controlled ballistic suborbital flight to study the most critical aerothermodynamic phenomena encountered during atmospheric reentry, and then will be recovered for postflight inspection [2,3]. EXPERT is expected to provide hypersonic flight conditions that could not be duplicated in existing hypersonic wind tunnels; in this way, a number of experiments will be carried out to study and validate aerothermodynamics models.

Among the scientific payloads, the vehicle will carry a hot structure made of ultrahigh-temperature ceramics (UHTC) [4]. Specific objectives of this payload are 1) to test UHTC (e.g., ZrB2/SiC) for future spacecraft at hypersonic reentry conditions (specific total enthalpy larger than 10 MJ/kg, surface heat flux on the order of 5–10 MW/m^2, and surface temperatures on the order of 2000°C); 2) to assess potential advantages related to the relatively high-emissivity and high-thermal conductivity that make UHTC particularly well suited for use as massive leading edges of sharp fuselages and wings (boundary-layer thermal protection) [5]; indeed, high heat flux levels can be tolerated with a relatively high thermal conductivity material that spreads the entering heat in the whole structure, lowering the temperature at the leading edge; 3) to investigate the behavior of UHTC at overall radiative equilibrium conditions; and 4) to investigate surface catalytic properties of UHTC with respect to recombination reactions in the presence of a highly dissociated oxygen mixture (through comparisons with plasma wind-tunnel results and with calculated and measured heat transfer rates).

As discussed in a previous paper [4], two winglets are symmetrically placed at the base of the reentry capsule (see Fig. 1) to study the behavior of different materials. The winglets are composed of a UHTC leading edge attached to an oxide dispersion strengthened (ODS) alloy support (PM 1000).

This paper is focused on the aerothermodynamic analysis (based on three-dimensional computations) carried out at the flight conditions along the EXPERT trajectory. The numerical model takes into account real gas properties, thermochemical nonequilibrium, and surface catalytic effects. The capsule–winglet aerodynamic interaction results in the boundary-layer separation and in the reattachment with a consequent heat flux increase at the winglet base [6]. A numerical model has also been prepared to simulate the fluid–structure thermal coupling to predict the temperature distribution along the reentry trajectory. One of the objectives of this paper is to analyze different thermal modeling of the UHTC hot structure to correctly predict its temperature during the reentry. In particular, the effect of thermal interaction with the capsule, the effect of thermal conductivity of the solid structure, the transient aerodynamic heating, and the effect of surface catalytic properties of the materials are investigated.

Received 9 July 2007; revision received 10 March 2008; accepted for publication 19 March 2008.

*Associate Professor, Aerospace Engineering Department, P.le Tecchio 80. Member AIAA.

†Research Assistant, Aerospace Engineering Department, P.le Tecchio 80. Member AIAA.

Fig. 1 Expert capsule configuration and winglet location.

II. Numerical Model

A. Computational Fluid Dynamics Solver

The computations have been performed with a state-of-the-art finite volume numerical code [7]. A number of user-defined subroutines have been developed to include different physical models and boundary conditions (see the following paragraphs).

The computational fluid dynamics (CFD) numerical model provides the solution of the equations of continuity, chemical species, momentum, energy, and vibrational energies for a steady, viscous reacting flow. Species viscosities, thermal conductivity, and mass diffusivities are derived from the kinetic theory of gases [8] as functions of the Lennard–Jones parameters. The solver computes the mixture viscosity and thermal conductivity with the semi-empirical Wilke's rule. The flow is considered as a five species mixture (N, O, N_2, O_2, NO). From the thermodynamic viewpoint, the system is considered a mixture of reacting ideal gases. In the present computations, the translational and rotational modes are in equilibrium at the temperature T, whereas polyatomic molecules may vibrate at a temperature T_v different from T. For the chemical reactions, the Park model [9] has been included, with the reaction rate constants specified by the Arrhenius law. For the vibration thermal relaxation, the Landau–Teller model was used [10].

At solid walls, the no-slip condition is enforced by setting the velocity components to zero. In chemically reacting flows, the mass fractions of the species are dependent variables with their transport equation. Species boundary conditions on the wall are assigned according to the behavior of the solid surface. For a fully catalytic wall, the chemical reactions are catalyzed at an infinite rate of reactions and the mass fractions are equal to their local equilibrium value. For a noncatalytic wall, the diffusive flux of atoms at the wall is set to zero. In addition, a user-defined function has been developed to simulate a wall with a finite value of surface catalycity, according to the following equation [11]:

$$\frac{\partial C_i}{\partial n} = \frac{C_i K_w}{D_i} \tag{1}$$

where n is the normal coordinate to the wall, K_w is the material catalytic constant function of the recombination coefficient $\gamma_w (0 \leq \gamma_w \leq 1)$ according to the equation:

$$K_w = \gamma_w \cdot \sqrt{\frac{R_0 T_w}{2\pi m_i}} \tag{2}$$

The vibration energy at the wall is set considering vibration thermodynamic equilibrium.

B. Computational Fluid Dynamics Code Validation

To show the code ability to predict hypersonic flows, two different classical test cases have been considered. A first problem, dealing with 3-D hypersonic shock/wave boundary-layer interaction, was considered. In particular, computations of hypersonic flow over an isothermal/adiabatic blunt fin junction have been carried out. This case was considered as a benchmark for high-speed flow computations during the First Europe-U.S. High Speed Flow Field Database Workshop [12]. The flat plate (Fig. 2) is set parallel to the freestream condition ($M_\infty = 3.92$, $P_0 = 1.26 \times 10^7$ Pa, $T_\infty =$ 456 K), the blunt fin ($210 \times 70 \times 6$ mm) with a leading-edge curvature radius of 3 mm is located on the flat plate 470 mm downstream of the plate leading edge in the half-span plane ($T_w = 300$ K).

For the present case [13], the Navier–Stokes equations have been solved for a turbulent flow under the assumptions of ideal gas computing the laminar viscosity with the Sutherland law. The turbulence model was the k-Ω (shear stress transport).

An $80 \times 80 \times 70$ grid has been generated, however, calculations were also performed on a $40 \times 40 \times 30$ mesh. The mesh was clustered to the walls, to ensure $y^+ < 0.5$ everywhere. The fin surface was supposed adiabatic, and a constant temperature $T_w = 300$ was assigned to the plate surface. The results show that the global flow properties are well predicted. The calculated pressure distributions show a fairly good agreement with experiments [14,15]. The sharp peak pressure and the local minimum pressure drop in the separated region, due to separated horseshoe vortex, are well predicted (Fig. 2a). The computed heat flux distribution is very close to the experimental in the region in front of the fin, but some differences occur in data on the lateral region. In any case, the peak heating and the local minimum heat flux drop in the separated region, which are the subject of the present benchmark, are fairly correctly predicted (Fig. 2b).

The hyperboloid flare (Fig. 3) is another test case considered to validate the numerical methodology employed for hypersonic flowfield simulations in high-enthalpy conditions. In the last few years, this benchmark was proposed during different high-speed flow

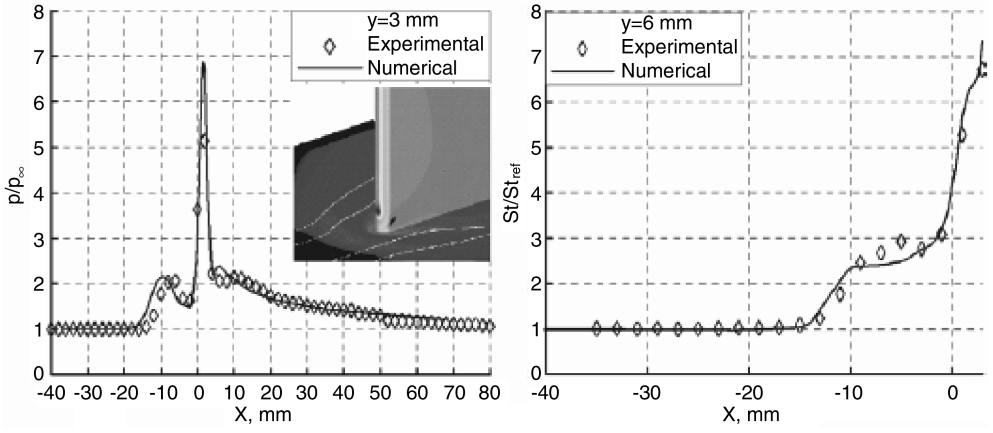

a) b)

Fig. 2 Computed and measured pressure a) and Stanton number b) distributions.

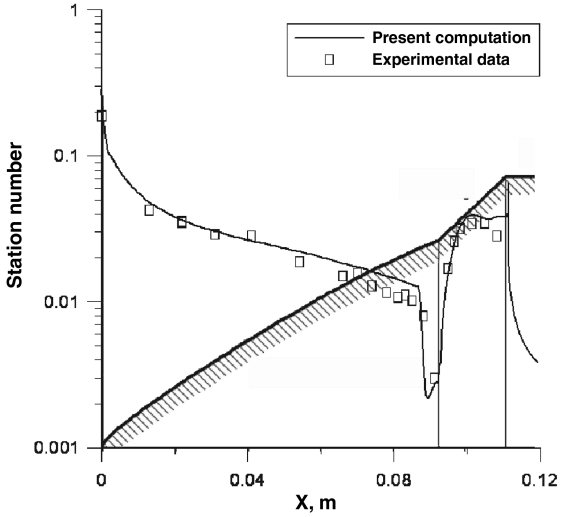

Fig. 3 Computed and measured Stanton number distributions on the hyperboloid wall.

workshops [16–18] due to the fact that complex physical phenomena are present and experimental results are available to validate numerical codes.

According to literature test case conditions [17], equations have been solved for a steady, axisymmetric, laminar flow under the assumptions of thermochemical nonequilibrium conditions ($M_\infty = 9.85$, $P_0 = 4.41 \times 10^7$ Pa, $H_\infty = 10.06$ MJ/kg). The hyperboloid flare configuration considered is shown in Fig. 3. The wall was assumed to be fully catalytic and the wall temperature is $T_w = 300$ K. The simulation has been computed using a grid of 474×110 cells, stretched (in the normalwise direction) around the stagnation point, to correctly predict the stagnation point heat flux, and near the corner (in the streamwise direction), to appropriately solve the shock wave/boundary-layer interaction.

The flowfield, in agreement with the experiments, is characterized by a little separated region with the corresponding cuspidlike shape of the Stanton number, typical of shock wave/boundary-layer laminar interaction. The Stanton number wall distribution is reported in Fig. 3 together with experimental data [18].

A similar test case on a blunted cone-flare was carried out by Savino and Paterna [19] in the frame of the FLOWNET test case database, with experimental conditions characterized by a low-enthalpy flow, therefore using the perfect gas model.

C. Computational Heat Transfer in Solids

The thermal analyses in the solid are carried out with the same finite volume code applied to CFD computations to numerically solve the heat conduction equation:

$$\frac{\partial}{\partial t}(\rho C_p T) = \nabla \cdot (k \nabla T) \tag{3}$$

where T is temperature, t is time, ρ is density, C_p is specific heat, and k is thermal conductivity. The thermal conductivity and the specific heat can be assumed to be temperature dependent. Furthermore, anisotropic thermal conductivity can be assigned by a conductivity matrix. The surface boundary conditions for transient aeroheating computations take into account both the convective and radiative heat fluxes.

D. Fluid–Solid Thermal Coupling

At the typical reentry conditions, if conduction in the solid is neglected (i.e., materials with very low thermal conductivity), local equilibrium is established between radiative and convective heat transfer, and the convective heat fluxes computed by CFD are sufficient to evaluate the body surface temperature referred as local radiative equilibrium temperature. When dealing with UHTC materials, characterized by relatively high thermal conductivity, the convective heat transfer to the surface is partly conducted to the solid and partly reradiated into the atmosphere. When a steady state is achieved, global radiative equilibrium is established, in the sense that the (surface) overall convective heat flux is perfectly balanced by the overall surface radiative flux.

During the steep reentry of the ballistic capsule, neither the local radiative equilibrium nor the global radiative equilibrium is achieved; the energy entering the surface by convection accumulates in the solid materials during the transient phase, in addition to being reradiated into the atmosphere and conducted through the solid.

To investigate the latter scenario, the numerical method is based on the following steps: 1) CFD simulations of the EXPERT capsule to identify the upstream conditions at the winglet location; 2) 3-D CFD simulations of the winglet at different points along the reentry trajectory to evaluate the heat fluxes on the structure; 3) 3-D heating simulations of the winglet during the reentry to evaluate the temperature distribution the hot structure.

A numerical model must be developed to relate the flowfield and the thermal field in the structure (steps 2 and 3). The different characteristic times for the fluid-dynamic and thermal phenomena suggest that it is possible to solve the flowfield around the body and the temperature field in the solid along the trajectory, with suitable coupling schemes. The fluid-dynamic equations and the energy equations in the solid can be solved "simultaneously" (coupled approach), or the fluid-dynamic equations can be solved only for some points of the vehicle trajectory, whereas the energy equation in the solid is solved for the entire trajectory (decoupled approach).

The latter method has been already numerically validated in a previous paper by Savino et al. [20] and will be followed in this work. This choice is dictated by the reduced computational time together with a sufficient accuracy. The computational procedure can be summarized in two phases:

1) Some CFD computations at relevant points of the trajectories must be performed with the freestream conditions at the winglet location obtained by capsule CFD computations. The normalized (nondimensional) three-dimensional convective heat flux distributions are obtained as

$$\frac{\dot{q}_c(x, y, z, t_i)}{\dot{q}_{\text{sp}}(t_i)} = \dot{q}_n(x, y, z) \tag{4}$$

where $\dot{q}_{\text{sp}}(t)$ is the heat flux at the stagnation point of the EXPERT capsule at the considered flight condition. These distributions are assumed to be similar at different trajectories points, so that one can consider $\dot{q}_n(x, y, z)$ constant along the trajectory, i.e., the winglet three-dimensional heat flux distribution will evolve according to the value of the EXPERT stagnation point heat flux.

2) The energy equation in the solid is solved, using the same finite volume code, in the time interval $(t, t + \Delta t)$, assuming as the boundary condition a time-dependent surface heat flux $q_{\text{in}}(t)$ entering the structure, obtained from convective heat flux, according to Eq. (4), minus the radiative heat flux:

$$q_{\text{in}}(x, y, z, t) = q_n(x, y, z) \cdot q_{\text{sp}}(t) \cdot \left(1 - \frac{c_p T_w(x, y, z, t)}{H_0(t)}\right) - \varepsilon \sigma T_w^4(x, y, z, t) \tag{5}$$

where $q_{\text{sp}}(t)$ changes according to an analytical formula [21], and $H_0(t)$ changes along the reentry trajectory.

This computation provides the new surface temperature distribution $T_w(t + \Delta t)$, which is then used in the next time step to update the surface heat flux $q_w(t + \Delta t)$ at the flight condition, corresponding to time $t + \Delta t$, also taking into account the change in surface heat flux due to change in surface temperature and to the radiative cooling.

To fit the CFD surface heat fluxes data to thermal analyses boundary conditions, the code interpolates the data mesh by a zero-order method. In other words, for each cell face of the solid conduction grid, the code uses the value from the mesh file

containing CFD data located closest to the cell face. Therefore, to obtain an accurate specification of the surface heat fluxes, the same winglet surface grid has been used both for CFD and thermal analyses computations.

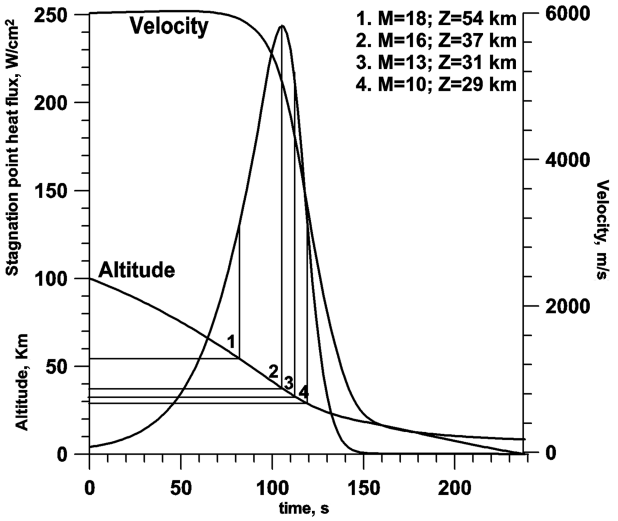

Fig. 4 EXPERT trajectory and CFD simulation points.

III. Winglet Model

A. Computational Fluid Dynamics Model

The incoming flow conditions for 3-D winglet computations were extracted from 3-D EXPERT computations 5 cm upstream of the winglet location in the frame of an ESA study [2] at different points along the reentry trajectory shown in Fig. 4. In particular, Mach number, temperature, pressure, and species mass fraction profiles have been assigned.

Figure 5 shows the comparison between the different simulated conditions of specific total enthalpy, Mach number, temperature, and atomic oxygen mass fraction. In particular, for the condition corresponding to the maximum heat flux (altitude of 37 km, $M = 16$) at 5 cm upstream of the winglet, the Mach number is about three, the temperature is about 2600 K, and the oxygen mass fraction is 0.23 (almost complete dissociation far from capsule boundary layer; as can be noted by Fig. 5, the capsule surface has been considered fully catalytic).

To obtain the normalized surface heat flux for different surface catalytic behavior (considered fixed along the reentry trajectory), the numerical computations have been carried out under the assumptions of a fully catalytic ($\gamma_w = 1$), partially catalytic ($\gamma_w = 0.1$), and noncatalytic surface ($\gamma_w = 0$). In all of the cases, the winglet and the plate have been assumed at a constant temperature $T_w = 300$ K.

Before the extensive computations performed in this work, a preliminary grid convergence analysis was carried out to find the best compromise between CPU time and results accuracy. Both grids (Fig. 6 shows the final configuration) are characterized by about

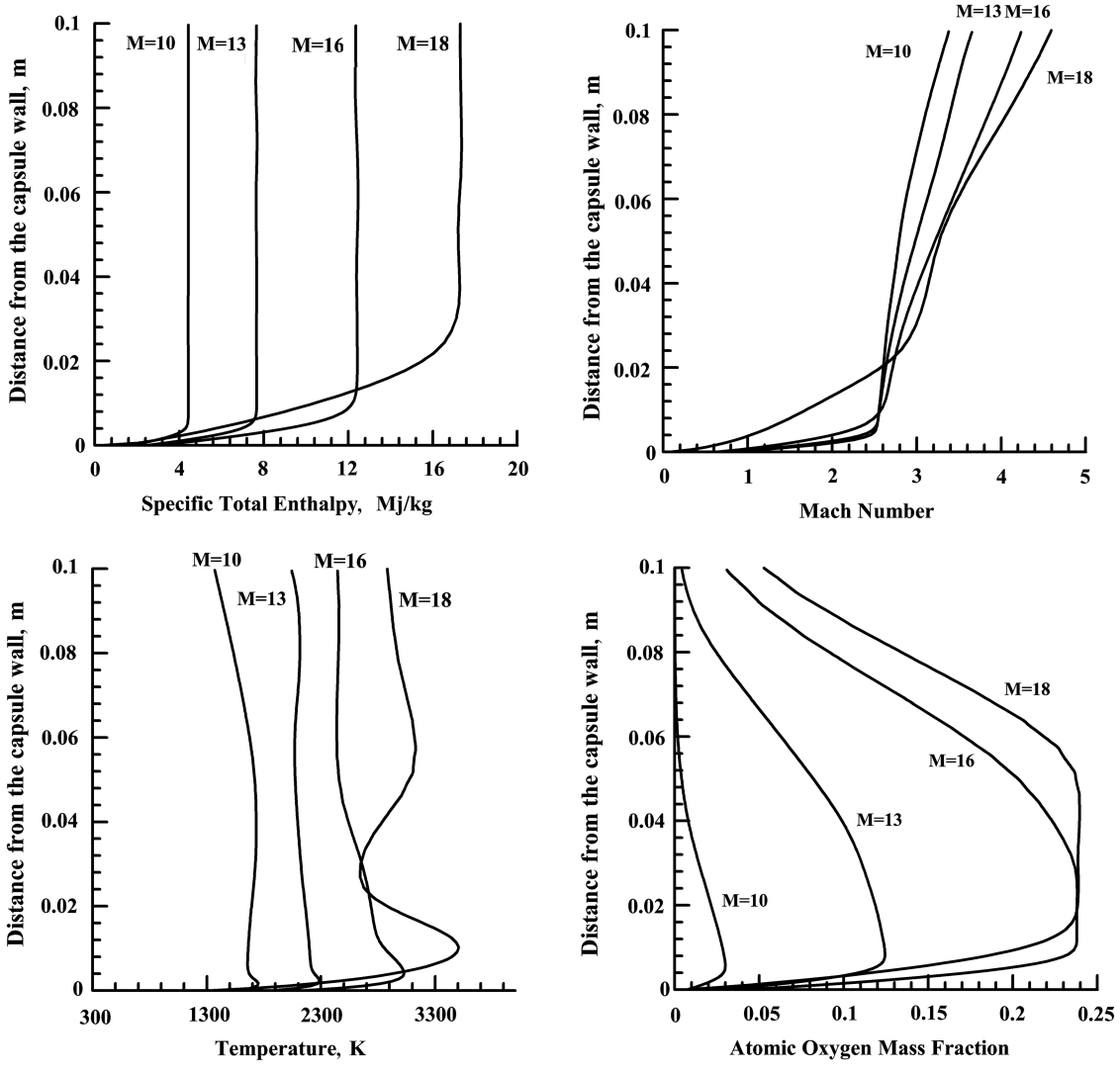

Fig. 5 Different profiles at the winglet location for the considered trajectory points.

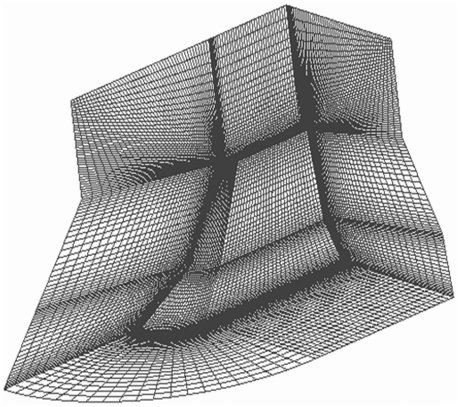

Fig. 6 Computational grid.

500,000 cells and are clustered near the wall ($\Delta y_w = 10^{-6}$ m) to correctly predict the surface heat fluxes.

B. Thermal Analysis Models

The thermal analysis was carried out with two different configurations: a preliminary case with the bottom wall of the winglet considered adiabatic (i.e., the winglet does not exchange heat with the capsule skin), and a more realistic configuration taking into account the winglet thermal interaction with the capsule skin (with different thicknesses of 2 and 10 mm). In this case, the aeroheating of the skin is also considered with the same procedure described in Sec. II.D. The plate dimensions are 30×30 cm (Fig. 7). The bottom wall and the side walls of the plate have been considered adiabatic. The relevant physical properties for the different solid materials (density, thermal conductivity, specific heat, and emissivity) are treated as constant over the expected range of temperatures and are summarized in Table 1 [22].

IV. Results

A. Flowfield Characteristics

Preliminary computations have been carried out to investigate the flowfield characteristics and to identify a suitable winglet geometry satisfying the scientific requirements. Figure 8 shows the two different configurations analyzed in the present paper. The first configuration (Fig. 8a) was tapered, with a swept angle of 45 deg. The curvature radius was 1 cm at the tip and 2 cm at the base, to reduce the heat load at the bottom according to the thermal constraints of the metallic support. The second and final configuration (Fig. 8b) is a double delta wing with swept angles of 25 and 55 deg. The curvature radius is 0.5 cm at the tip and 2 cm at the base. The overall length of both configurations is 10 cm, and the height is 5 cm in both cases.

Figures 9a and 9b show pressure contours, skin friction, and surface heat flux profiles for the preliminary and final configurations in Fig. 9, corresponding to the maximum aeroheating conditions (altitude of 37 km, $M_\infty = 16$; see Fig. 4). These results are obtained in laminar condition with thermochemical nonequilibrium. The

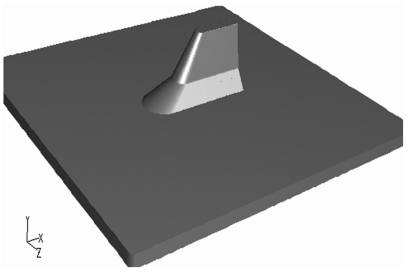

Fig. 7 Thermal model with winglet–capsule skin thermal interaction (final configuration).

Table 1 Physical properties of the materials

Properties	ZrB_2	ODS
Density, kg/m^3	6000	8300
Thermal conductivity, $W/m \cdot K$	66	14.26
Specific heat, $J/kg \cdot K$]	628	400
Emissivity, –	0.8	0.8

maximum pressure is higher in the final configuration due to the higher second swept angle (60 deg) compared with the preliminary one (45 deg).

In the final configuration, the stronger shock wave is mainly located on the upper part of the winglet, where high temperatures occur. The bottom part of the winglet is, in this case, exposed to lower heat fluxes, and this is beneficial to avoid high temperatures at the junction with the capsule wall. Keeping in mind that one of the objectives of the mission is to achieve large temperatures on the UHTC preserving the capsule structure, the choice of the double delta configuration is justified by the larger heat flux on the top of the winglet and lower heat flux near the capsule. The tapering of the winglet, which reduces the radius of curvature from 1 to 0.5 cm on the top of the leading edge, increases the surface heat flux (due to the well-known law of the inverse of the square root of the radius of curvature). In addition, the higher swept angle on the top, with respect to the preliminary configuration, leads to a further increase of heat flux (due to the dependence of the heat flux on the swept angle [12]).

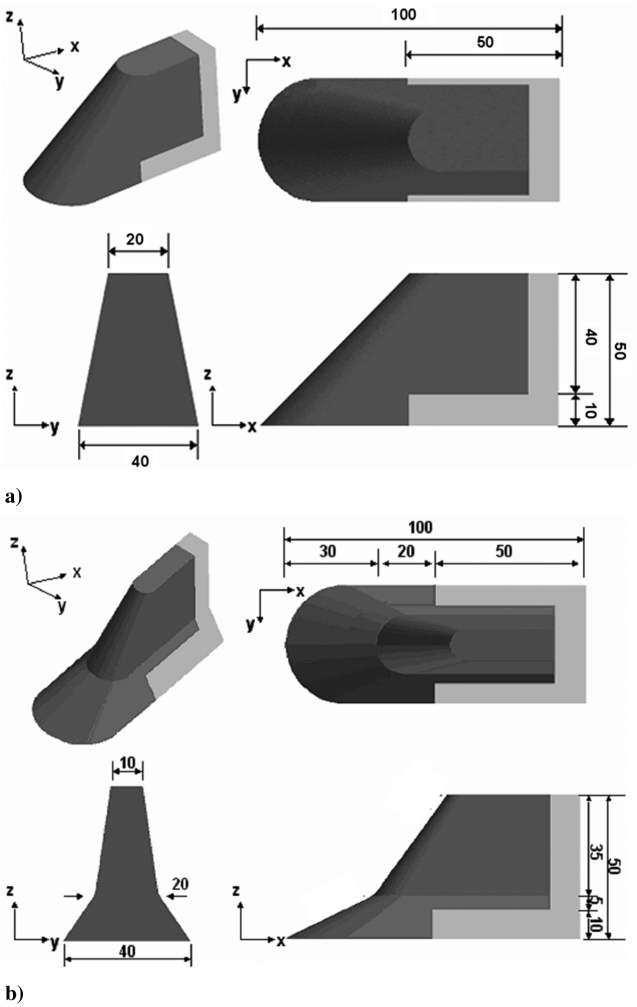

Fig. 8 Geometries of the winglet (dimensions in millimeters): a) preliminary configuration, b) final configuration.

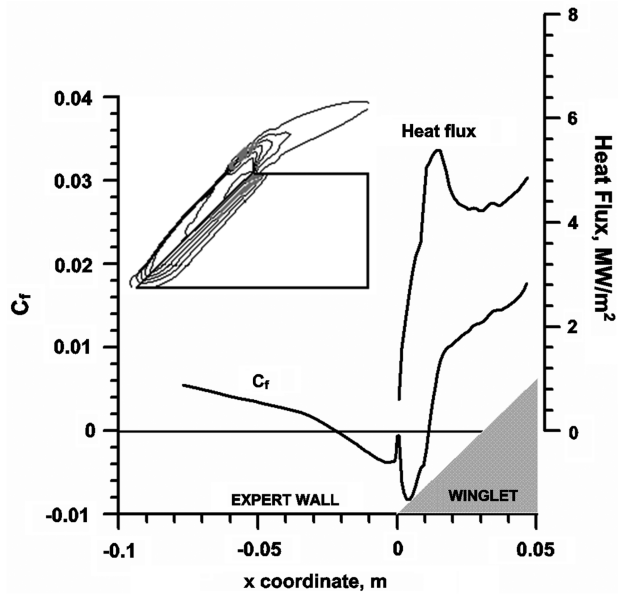

a)

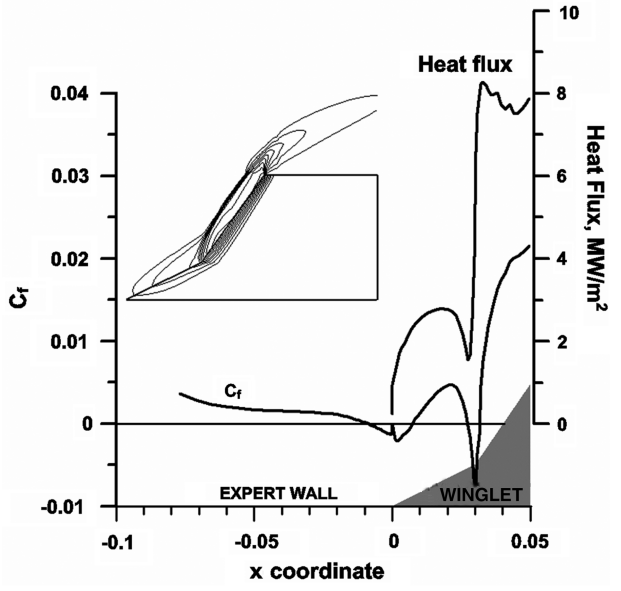

b)

Fig. 9 Symmetry plane. Pressure contours, skin friction, and surface heat flux profiles: a) preliminary configuration, b) final configuration.

B. Time Evolution of Temperature Distributions During Reentry

The results of CFD simulations performed at different altitudes of the trajectory (between 40 and 30 km, which is the maximum heating range) pointed out (as reported in the Sec. II.D) that the normalized heat flux can be considered constant. Therefore, a decoupled approach was applied for the thermal analysis. The preliminary analysis was carried out considering the winglet as a fully catalytic surface and the base was supposed adiabatic (i.e., the heated winglet was not thermally coupled with the capsule). Of course, this assumption is the worst case in terms of winglet heating.

Figure 10 shows the surface heat fluxes at different times during the reentry for the preliminary winglet configuration and the corresponding surface temperatures. The region of maximum surface heat flux is located near the bottom region of the leading edge. This can be explained by the shock–boundary-layer interaction resulting in the separation and reattachment of the laminar boundary layer on the capsule surface, as observed in the Sec. IV.A. The maximum value of the surface temperature along the trajectory is about 2300 K.

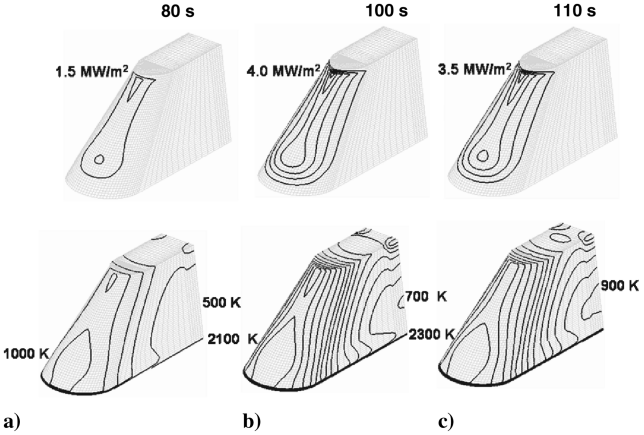

a) b) c)

Fig. 10 Surface heat flux a) maximum value, $\Delta\dot{q} = 0.5$ MW/m^2, and temperatures b) maximum and minimum value, $\Delta T = 100$ K at different times along reentry.

During these preliminary computations, the effect of the thermal coupling with the capsule has been investigated. A plate with two different thickness (2 mm and 1 cm) have been modeled to evaluate the effect of the conduction in the capsule shell.

Table 2 shows the maximum temperature values on the tip and on the root of the winglet for the different capsule skin thermal coupling conditions. As can be noted, the increase of plate thickness reduces the maximum heating of the winglet and shifts the maximum temperature spot on the winglet tip. Anyway, the winglet temperatures are too low on the UHTC to achieve the required temperatures and too large on the capsule skin (temperatures larger than 1450 K are not admissible for system requirements).

Figure 11 shows the surface heat fluxes at different times during the reentry for the final configuration considering the thermal coupling with the capsule skin of 2 mm of thickness. As a result of the change of the geometry, compared with the initial configuration (see Fig. 10), the region of maximum surface temperature is now located on the top of the leading edge with a maximum value of about 2600 K (for a fully catalytic wall). This value is very high, but on the order of the maximum allowable temperature for UHTC materials, according to the most recent arc-jet tests [23].[‡]

It is interesting to compare the results obtained by transient analyses with the results obtained by CFD simulations considering the radiative equilibrium condition (neglecting the thermal conduction and assuming on the wall the condition $q_c = \varepsilon\sigma T_w^4$) and with the numerical computation of the steady state (Fig. 12) achieved by imposing the maximum surface heat fluxes distributions obtained by CFD ($Z = 37$ km, $M = 16$) and considering the effect of thermal conduction until global radiative equilibrium conditions is achieved. The difference of these results can be attributed to two different effects: the large thermal conductivity of the UHTC materials and the transient surface heat flux boundary conditions due to trajectory evolution.

It is clear that, to correctly predict the thermal field of a relatively large conductivity massive material along a reentry trajectory, a

Table 2 Capsule skin thermal coupling effect

	Adiabatic root	2 mm thickness plate	10 mm thickness plate
Maximum tip temperature, K	1950	1910	1900
Maximum root temperature, K	2230	1970	1550

[‡]TPS-X database Web site, NASA Ames Research Center, http://tpsx.arc.nasa.gov.

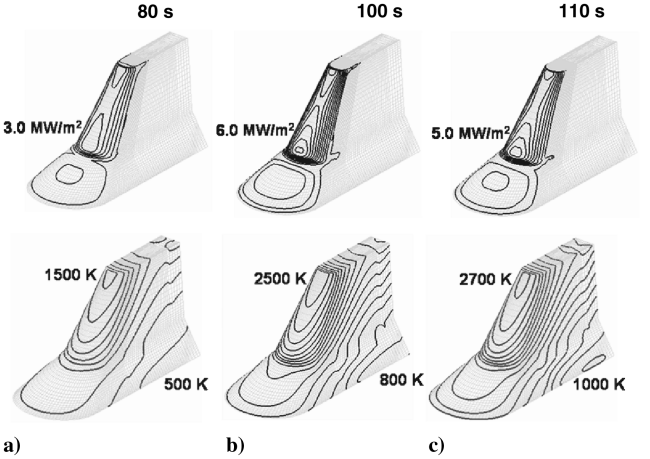

Fig. 11 Surface heat flux a) maximum value, $\Delta\dot{q} = 0.5$ MW/m^2, and temperatures b) maximum and minimum value, $\Delta T = 100$ K at different times along reentry.

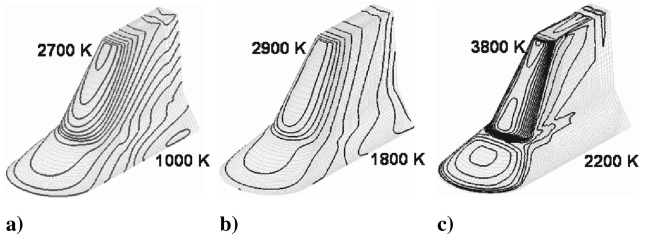

Fig. 12 Maximum surface temperatures for a) thermal analysis along trajectory, b) steady state at the maximum heating conditions, and c) CFD radiative equilibrium (maximum and minimum value, $\Delta T = 100$ K).

thermal analysis, taking into account the evolution of the surface heat fluxes along the trajectory, is necessary to avoid an excessive overestimation of results.

C. Surface Catalicity Effect

All the simulations presented before have been carried out considering a fully catalytic wall. This condition implies that all of the atomic species, generated across the bow shock of the EXPERT nose (no atomic recombination occurs in the flowfield behind the bow shock), flow in the winglet region and recombine completely at the surface. Of course, this phenomenon depends on the surface catalysis properties of the UHTC materials, which unfortunately are not known in all of the interested range of pressure and temperature. A sensitivity analysis of the surface catalysis has been performed to identify how this property affects the surface temperature values on the winglet along the reentry trajectory.

Table 3 summarizes the maximum computed cold wall surface heat flux and the temperatures on the winglet for a fully catalytic (FC), partially catalytic (PC), and noncatalytic (NC) wall, for the condition of maximum aeroheating (altitude of 37 Km, $M = 16$). For the case of a partially catalytic wall, a value of the recombination factor $\gamma_w = 0.1$ has been considered [24]. The skin surface of the capsule has been considered in all the computations as a fully catalytic wall in accordance with PM1000 behavior.

Table 3 Surface catalysis effect

	NC	PC ($\gamma_w = 0.1$)	FC
Maximum surface heat flux, MW/m^2 ($Tw = 300$ K)	5.88	7.35	9.80
Maximum surface temperature, K (thermal analysis)	2080	2420	2650

The maximum value of the surface temperature achieved by means of transient thermal analyses using normalized surface heat fluxes, as defined in Sec. II.D, are in the range of between about 2600 K, as already seen in Fig. 11, for a fully catalytic wall and about 2080 K for a noncatalytic wall. In both cases, the temperature of the metallic support does not exceed its maximum allowable value.

V. Conclusions

The aerothermodynamic analysis of the winglet developed for the EXPERT mission have been carried out, taking into account the complex chemical and vibration nonequilibrium phenomena, the partial catalytic properties of the surface, the wall radiation, and the thermal fluid–structure interaction by means of a number of user defined functions to customize the numerical code, which was validated by means of comparisons with experimental data for hypersonic flow benchmarks. The aerothermal analysis provides surface temperature distributions that are strongly dependent on the coupling with the capsule skin and on the surface catalytic properties of the UHTC materials. According to the scientific requirements, the final configuration design is able to provide surface temperatures larger than 2000 K on the UHTC leading edge also for a noncatalytic wall and allowable temperatures on the metallic support in the worst case of a fully catalytic wall. Before the flight, qualification tests will be carried out in the SCIROCCO Plasma Wind Tunnel available at the Italian Aerospace Research Center.

Acknowledgments

The authors would like to thank G. Marino and R. Gardi of the Italian Aerospace Research Center for their valuable effort in the design and development of the Payload 15–Sharp Hot Structures in the frame of the ESA European experimental reentry test bed program.

References

[1] Muylaert, J., Cipollini, F., Tumino, G., Kordulla, W., Saccoccia, G., and Stravinidis, C., "Preparing for Atmospheric Reentry with EXPERT's Help," ESA Bulletin No. 114, 2003, pp. 42–48.

[2] Walpot, L., and Ottens, H., "FESART/EXPERT Aerodynamic and Aerothermodynamic Analysis of the REV and KHEOPS Configuration," ESA European Space Research and Technology Center TR TOS-MPA/2718/LW, 2002.

[3] Ottens, H., and Walpot, L., "EXPERT Model 4.2, Model Description and Trajectory Analysis," ESA European Space Research and Technology Center TR TOS-MPA/2749/HO, 2003.

[4] Savino, R., De Stefano Fumo, M., Marino, G., and Tului, M., "Aerothermal Analysis of an Advanced Hot Structure for Hypersonic Flight Tests," *Materials for Space Application*, Vol. 851, edited by M. Kipara, D. L. Edwards, R. S. Benson, and S. Philips, Materials Research Society, Warrendale, PA, 2005.

[5] Monti, R., Pezzella, G., Savino, R., Paterna, D., and Esposito, A., "Aerothermodynamic Study of an Advanced Thermal Protection System, Hot Structures and Thermal Protection System for Space Vehicles," *Proceedings of the 4th European Workshop*, edited by A. Wilson, ESA, 2002, p. 275.

[6] Anderson, J. D., Jr., *Hypersonic and High Temperature Gas Dynamics*, AIAA, Reston, VA, 2000.

[7] "Fluent 6.2 User's Guide," Fluent, Lebanon, NH, 2004.

[8] Hirscfelder, J. O., Curtiss, C. F., and Bird, R. B., *Molecular Theory of Gases and Liquids*, Wiley, New York, 1954, pp. 75–106.

[9] Park, C., "Review of Chemical-Kinetic Problems of Future NASA Missions, 1: Earth Entries," *Journal of Thermophysics and Heat Transfer*, Vol. 7, No. 3, 1993, pp. 385–398.

[10] Millikan, R. C., and White, D. R., "Systematics of Vibrational Relaxation," *Journal of Chemical Physics*, Vol. 39, No. 12, 1963, pp. 3209–3213.
doi:10.1063/1.1734182

[11] Suslov, O. N., and Tirskiy, G. A., "Kinetics of the Recombination of Nitrogen Atoms on High Temperature Reusable Surface Insulation in Hypersonic Thermo-Chemical Non-Equilibrium Flow, Aerothermodynamics for Space Vehicles," *Proceedings of the 2nd European Symposium*, edited by J. J. Hunt, ESA, 1995, p. 413.

[12] Batten, P., Loyau, H., and Leschziner, M. A., Computation of the HSSF T5-97.2 Blunt Fin Test Case, *Proceedings of the 1st Europe-US High Speed Flow Field Database Workshop, Part 2*, Italian Aerospace Research Center with permission of AIAA, Naples, 1997, pp. 317–323.

[13] Marini, M., Description of Test Cases, *Proceedings of the 1st Europe-US High Speed Flow Field Database Workshop, Part 2*, Italian Aerospace Research Center with permission of AIAA, Naples, 1997, pp. 1–56.

[14] Fox, J. S., O'Byrne, S., Houwing, A. F. P., Papinniemi, A., Danhey, P. M., and Mudford, N. R., "Fluorescence Visualisation of the Hypersonic Flow Establishment over a Blunt Fin," *AIAA Journal*, Vol. 39, No. 7, 2001, pp. 1329–1337.

[15] Aso, S., Tan, A., and Hayashi, M., "Structure of Aerodynamic Heating in Three-dimensional Shock Wave/Boundary Layer Interaction Induced by Sharp and Blunt Fins," AIAA Paper 89-1854, 1989.

[16] Grasso, F., Marini, M., and Morinischi, K., Description of Test Cases, *Proceedings of First Eastern-Western High Speed Flow Field Database Workshop*, AIAA, Reston, VA, 1998, pp. 1–48.

[17] Marini, M., Contribution to T1-97 Hyperboloid Flare Problems, *Proceedings of First Europe-US High Speed Flow Field Database Workshop, Part 2*, Italian Aerospace Research Center with permission of AIAA, Naples, 1997, pp. 301–323.

[18] Sagnier, P., Joly, V., and Marmignon, C., "Analysis of Non Equilibrium Flow Calculations and Experimental Results Around a Hyperboloid-Flare Configuration, Aerothermodynamics for Space Vehicles," *Proceedings of the 2nd European Symposium*, edited by J. J. Hunt, ESA 1995, pp. 491–496.

[19] Savino, R., and Paterna, D., "Blunted Cone-Flare in Hypersonic Flow," *Computers and Fluids*, Vol. 34, No. 7, 2005, pp. 859–875. doi:10.1016/j.compfluid.2004.05.012

[20] Savino, R., De Stefano Fumo, M., Paterna, D., and Serpico, M., "Aerothermodynamic Study of UHTC-Based Thermal Protection Systems," *Aerospace Science and Technology*, Vol. 9, No. 2, 2005, pp. 151–160. doi:10.1016/j.ast.2004.12.003

[21] Tauber, M. E., "Review of High-Speed Convective, Heat Transfer Computation Methods," NASA Technical Paper 2914, 1989.

[22] Rasky, D. J., "Advanced Ceramic Matrix Composites for TPS, Current Technology for Thermal Protection System," NASA CP-3157, 1992.

[23] Monteverde, F., and Savino, R., "Stability of Ultra-High-Temperature ZrB2-SiC Ceramics Under Simulated Atmospheric Re-Entry Conditions," *Journal of the European Ceramic Society*, Vol. 27, No. 16, 2007, pp. 4797–4805. doi:10.1016/j.jeurceramsoc.2007.02.201

[24] Marschall, J., Chamberlain, A., Crunkleton, D., and Rogers, B., "Catalytic Atom Recombination on ZrB2/SiC and HfB2/SiC Ultrahigh-Temperature Ceramic Composites," *Journal of Spacecraft and Rockets*, Vol. 41, No. 4, 2004, pp. 576–581. doi:10.2514/1.2879